

Solvent-Modulated Luminescent Spheroidal Assemblies of Cu₈ Nanocluster for Volatile Amine Sensing

Subrata Duary, Arijit Jana, Amitabha Das, Ankit Sharma, Biswarup Pathak,*
Kumaran Nair Valsala Devi Adarsh,* and Thalappil Pradeep*



Cite This: <https://doi.org/10.1021/acs.inorgchem.5c01082>



Read Online

ACCESS |



Metrics & More

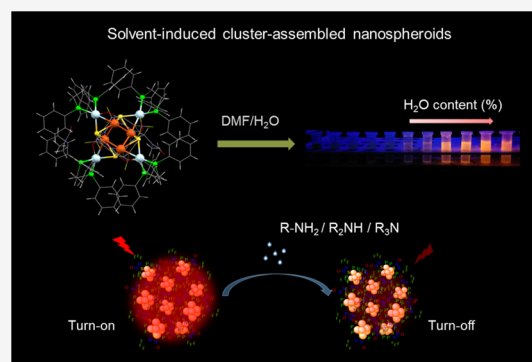


Article Recommendations



Supporting Information

ABSTRACT: Cluster-assembled luminescent microstructures built with metal nanoclusters (NCs) represent a promising class of nanomaterials with diverse applications in photonics and sensing. In this work, we have designed a strategy to make a photoluminescent material by assembling atom-precise NCs of [Cu₈(TFMPT)₄(DPPE)₄] (abbreviated as Cu₈), where TFMPT is 4-hydroxy-6-(trifluoromethyl) pyrimidine-2-thiolate and DPPE is 1,2-bis(diphenylphosphino)ethane. Single-crystal X-ray diffraction (SC-XRD) reveals a unique tetracapped tetrahedral Cu₈ core structure. Upon gradual addition of water (50–85 vol %) to the visibly nonluminescent dimethylformamide (DMF) solution of the clusters, a strong orange luminescence (emission at 625 nm under ultraviolet (UV) light) was observed. It is due to the formation of spheroidal assemblies of nanometer dimension. The cluster-assembled spheroids (CASs) are formed due to hydrophobic interactions among clusters as the concentration of water increases in the solution. Time-correlated single-photon counting reveals that the lifetime of luminescent aggregates is on a microsecond scale, which suggests phosphorescence. Such phosphorescent CASs show a fast response, high selectivity, and naked-eye detection of volatile amines (VAs). Spectroscopic studies and density functional theory (DFT) calculations provide an in-depth understanding of luminescence quenching of CASs and a mechanistic understanding of ammonia and trimethyl amine sensing. The limits of detection (LoD) of ammonia and trimethyl amine were measured to be 0.568×10^{-7} M (0.001 ppm) and 0.362×10^{-7} M (0.002 ppm), respectively. Overall, apart from enriching the family of copper clusters, this work additionally introduces a new photoluminescent material for volatile organic amine (VOA) compound sensing of environmental relevance.



INTRODUCTION

Atomically precise noble metal nanoclusters (NCs) of size below ~ 3 nm belong to a class of novel nanomaterials, endowed with molecule-like discrete energy levels, photoluminescence, chirality, magnetism, etc.¹ In the last two decades, intense efforts on the synthesis, characterization, and diverse applications of silver and gold NCs have been reported. However, copper NCs have received comparatively less attention due to the easy oxidation of copper under air (E^0 values of Au⁺/Au, Ag⁺/Ag, and Cu⁺/Cu are 1.69, 0.79, and 0.52 V, respectively).² Notwithstanding this limitation, Cu NCs need to be explored because of their earth abundance and consequently low cost, nontoxicity, and high catalytic activity. Tuning the synthesis and crystallization methods has been used intensely to obtain the structures of several small and moderately sized copper clusters (e.g., Cu₄, Cu₅, Cu₈, Cu₁₂, Cu₁₄, Cu₁₅, Cu₂₃, Cu₂₅, Cu₆₁, Cu₈₁, Cu₉₃, Cu₉₆, and Cu₁₃₆) with appropriate ligand protection.^{3–10}

Photoluminescence is one of the fascinating properties of ultrasmall noble metal NCs used for applications in nanophotonics and optical sensing. Copper clusters with intense

emission, good photostability, and high yield of synthesis make them promising luminescent materials for optoelectronic applications.^{11,12} Such luminescent Cu NCs show similar characteristics such as large Stokes shift and long emission lifetimes in comparison to the conventional luminescent materials (organic dyes and semiconductor quantum dots).^{13–15} To enhance the photoluminescence of such clusters, researchers have used several approaches such as surface functionalization, alloying, host–guest interaction, and aggregation-induced emission (AIE).^{16–21,26} Out of such approaches, AIE occurs very frequently for Cu NCs. In the aggregated state of clusters, metallophilic interactions, restricted motion of ligands, and enhanced radiative relaxation pathways result in enhanced photoluminescence intensity

Received: March 8, 2025

Revised: May 8, 2025

Accepted: May 13, 2025

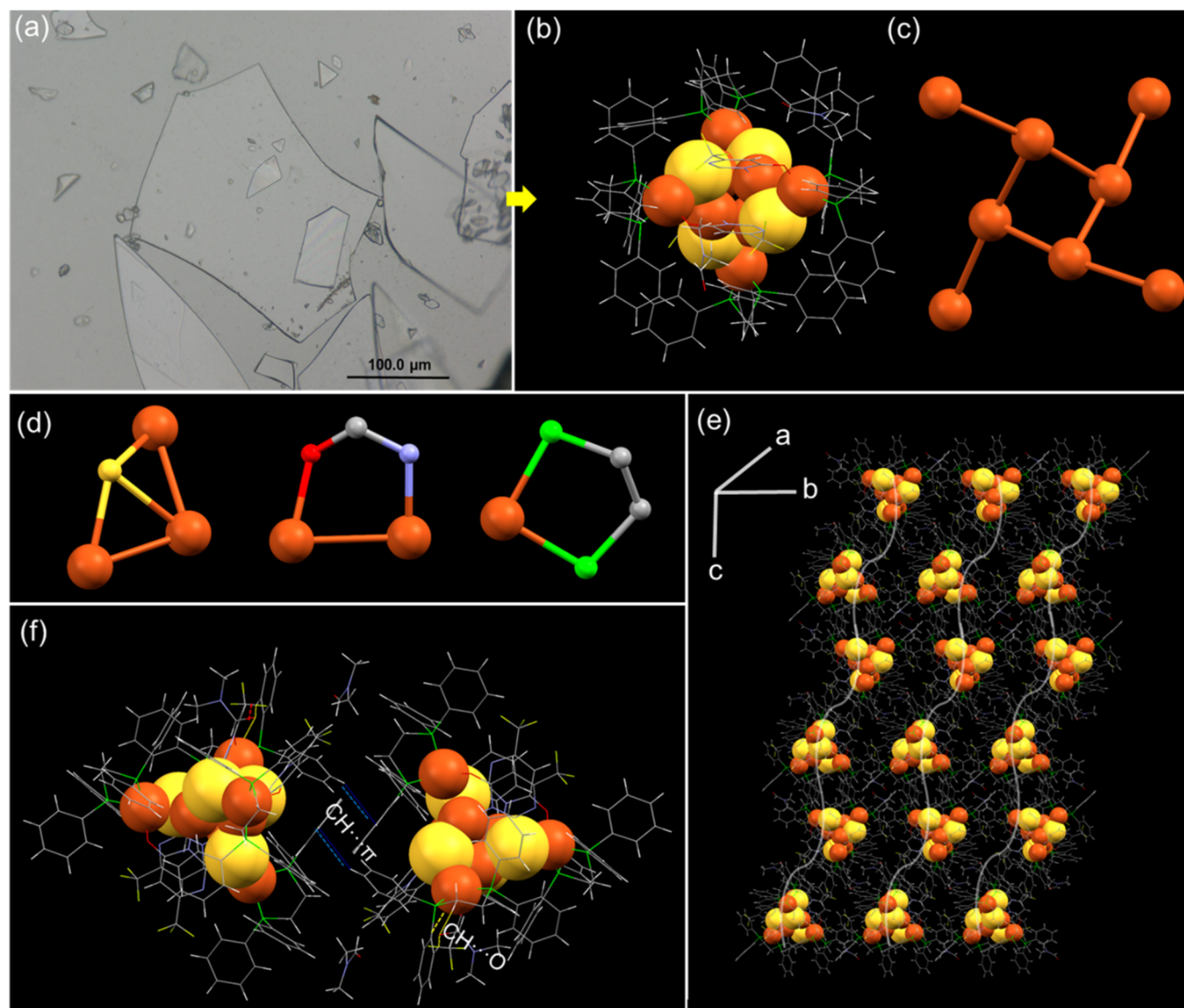


Figure 1. (a) Optical images of single crystals of the Cu_8 nanocluster (scale bar $100 \mu\text{m}$). (b) Full structure of ligand-protected Cu_8 cluster (hydrogens are removed for clarity) with crystallized DMF molecules. (c) Cu_8 core structure. (d) Binding sites of ligand part to Cu. (e) Structured packing ($3 \times 3 \times 3$) of Cu_8 nanocluster along the a -axis. (f) Different noncovalent interactions within ligands and crystallized DMF molecules. Atomic color code: orange = Cu, yellow = S, green = P, gray = C, red = O, blue = N, light green = F, and white = H.

compared with isolated NCs.²⁶ The aggregation phenomenon is driven by intercluster interactions or electrostatic attractions (dipole–dipole, hydrogen bonding, metallophilic interactions, and hydrophobic interactions) arising through ligands.^{22–25} The emission wavelength in such aggregates is highly determined by interatomic distances and compactness of assembled metal NCs.²⁶ The origin of photoluminescence due to the aggregation and self-assembly of metal NCs is a burgeoning area of research.

Recently, cluster-assembled materials have emerged as promising candidates for various sensing applications, related to environmental contamination and human health.^{27–29} Nowadays, environmental contamination due to the release of volatile organic amine (VOA) compounds from industrial fertilizers and biological degradation processes is a matter of concern to public health and water bodies.^{30,31} Although there are many analytical techniques available for their detection such as high-performance liquid chromatography, gas chromatography–mass spectrometry, capillary electrophoresis,

Raman scattering, and electrochemical methods, new strategies are essential for efficient detection of VOAs.³² This is made possible by the discovery of highly sensitive materials.

In this work, we have synthesized a copper nanocluster $[\text{Cu}_8(\text{TFMPT})_4(\text{DPPE})_4]$ following the strategy of ligand-exchange-induced structural transformation (LEIST), where TFMPT is 4-hydroxy-6-(trifluoromethyl) pyrimidine-2-thiolate and DPPE is 1,2-bis(diphenylphosphino)ethane. The cluster in dimethylformamide (DMF) was crystallized by the slow evaporation of solvent at ambient temperature. The Cu_8 core is composed of a unique tetracapped tetrahedral geometry. Interestingly, the Cu_8 cluster, which remains nonemissive in both solid and solution states, displays intense orange luminescence when mixed with water (vol %, 50–85%). The origin of luminescence is attributed to the formation of cluster-assembled spheroids (CASs). Such CASs exhibit “turn-off” luminescence in the presence of amines (liquid and vapor) due to the binding of such molecules with clusters. Altogether, this work presents an unexplored Cu_8 nanocluster manifesting

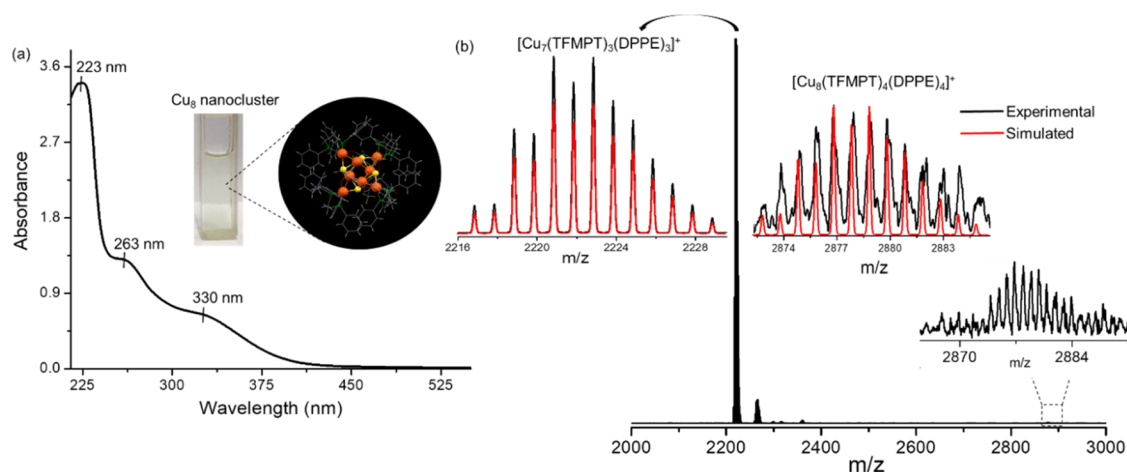


Figure 2. (a) UV-vis absorption spectrum of Cu_8 nanocluster in acetonitrile, inset photographic images of the cluster in acetonitrile and full structure. (b) Full-range high-resolution ESI-MS of Cu_8 nanocluster in positive mode; inset shows exact matching of experimental (black) and simulated (red) spectra. Inset shows the molecular ion peak at low abundance.

solvent-induced aggregation and the use of resulting assemblies for amine sensing.

RESULTS AND DISCUSSION

Synthesis and Characterization. The $[\text{Cu}_8(\text{TFMPPT})_4(\text{DPPE})_4]$ nanocluster, abbreviated as Cu_8 , was synthesized under ambient conditions following the LEIST reaction, starting from the $[\text{Cu}_{18}\text{H}_{16}(\text{DPPE})_6]^{2+}$ (abbreviated as Cu_{18}) nanocluster. The synthesis protocol is described in the **Experimental Section**. The precursor Cu_{18} NC was synthesized following an earlier report.³³ Essential characterization of the Cu_{18} NC is covered in **Figure S1**. Synthesized Cu_8 cluster was crystallized as colorless sheet-like single crystals from the reaction mixture via slow evaporation of the solvent DMF under ambient conditions (**Figure 1a**).

Single Crystal Structure. The molecular structure of the cluster was determined by single-crystal X-ray diffraction (SC-XRD). The field emission scanning electron microscopy (FESEM) micrograph (gold sputtered on single crystals to reduce charging effect and improve image contrast) further verified the sheet-like surface morphology of the crystals (**Figure S2a**), and energy dispersive spectroscopy (EDS) elemental mapping shows the atomic composition as Cu (3.22%), S (0.96%), N (2.92%), O (22.08%), P (1.73%), and F (3.99%) (**Figure S2d**). SC-XRD reveals that Cu_8 was crystallized in a triclinic crystal system with the space group of *P*-1 having a cell volume of 6510.8 \AA^3 (brief crystallographic details are summarized in **Table S1** in SI). The ORTEP representation of the Cu_8 cluster is drawn at the 50% probability level showing the arrangement of copper atoms (**Figure S8**). The Cu_8 cluster core is composed of two interpenetrating puckered Cu_6S_2 units. Some reports suggest that most of the Cu_8 cluster cores are branched chain, fused tetrahedron, or cubic (summarized in **Figure S3**).^{35–40} We report a tetracapped distorted tetrahedral Cu_8 core structure, distinctly different from those known already (**Figure 1b**). The entire molecular structure contains a Cu_8 kernel protected by 1:1 thiol (TFMPPT- H_2) and phosphine (DPPE). The inner $[\text{Cu}_4]_{\text{td}}$ is protected by four units of $\text{Cu}(\text{HTFMP})(\text{DPPE})$ making a compact Cu_8S_4 core. Each Cu atom of the outer $[\text{Cu}_4]_{\text{td}}$ is coordinated by one DPPE ligand. Careful analysis of single crystal structure indicates that thiols play a unique role

in stabilizing the core structure. The N and O sites of thiol coordinate to inner and outer Cu, respectively, which provides rigidity to the core. The Cu–Cu distance in the inner $[\text{Cu}_4]$ unit is $2.572\text{--}2.596 \text{ \AA}$, which is slightly longer than that in bulk copper. All S atoms are μ_3 bridging and the Cu–S distance is $2.240\text{--}2.386 \text{ \AA}$ (**Figure S4e**). The Cu–N, Cu–O, and Cu–P bond distances are $1.991\text{--}1.998$, $2.042\text{--}2.078$, and $2.235\text{--}2.386 \text{ \AA}$, respectively (**Figure S4f–h**). In the Cu_8S_4 framework, copper and sulfur are arranged in tetrahedral units ($[\text{Cu}_4]_{\text{inner}}@S_4@[\text{Cu}_4]_{\text{outer}}$). Two molecules are present in each unit cell (**Figure S4a**). We observed two cocrystallized DMF molecules with one Cu_8 cluster (**Figure 2b**). In the extended lattice, clusters are packed through noncovalent interactions such as $\text{CH}\cdots\text{O}$, $\text{CO}\cdots\text{F}$, $\text{CH}\cdots\pi$, $\text{CH}\cdots\text{F}$, and $\text{CH}\cdots\text{CH}$ with distances of 2.57 , 2.98 , 6.87 , 2.414 , and 2.184 \AA , respectively (**Figure 1f**). These interactions contribute to the stabilization and organization of the clusters within the crystal lattice (**Figure 1e**).

Other Characterization Data. The UV-visible (UV-vis) absorption spectrum of Cu_8 NC in acetonitrile (ACN) shows three absorption peaks at 223, 263, and 330 nm, respectively (**Figure 2a**). The absorption features of the cluster in ACN show stability for up to 15 days (**Figure S5**). High-resolution ESI-MS spectrum in the positive ion mode shows a molecular ion peak at m/z 2878.65 (**Figure 2b**), which is assigned to $[\text{Cu}_8(\text{TFMPPT})_4(\text{DPPE})_4]^+$. Another peak was observed at m/z 2225.53 (1+), which corresponds to the molecular composition, $[\text{Cu}_7(\text{TFMPPT})_3(\text{DPPE})_3]^+$. The isotopic distributions of the experimental and theoretical spectra agreed well with each other (inset of **Figure 2b**). Upon an increase in the collision energy (CE), thiol and phosphine losses were observed from $[\text{Cu}_7(\text{TFMPPT})_3(\text{DPPE})_3]$ (**Figure S6**). X-ray photoelectron spectroscopy (XPS) analysis shows the presence of all elements in the crystal structure of Cu_8 NC, as described in **Figure S7**. The spectral regions of Cu $2p_{3/2}$ and $2p_{1/2}$ at 932.5 and 952.4 eV, respectively, suggested the presence of mixed Cu^0 and Cu^1 oxidation states, which were also supported by the Cu LMM Auger peak at 570 eV (inset of **Figure S7**). Such types of oxidation states in copper nanoclusters were also previously reported.^{5,34} Fourier transform infrared (FTIR) spectroscopy study indicates the binding of ligand to cluster core (**Figure S9**). The vibrational signal of $-\text{SH}$ ($\sim 2565 \text{ cm}^{-1}$)

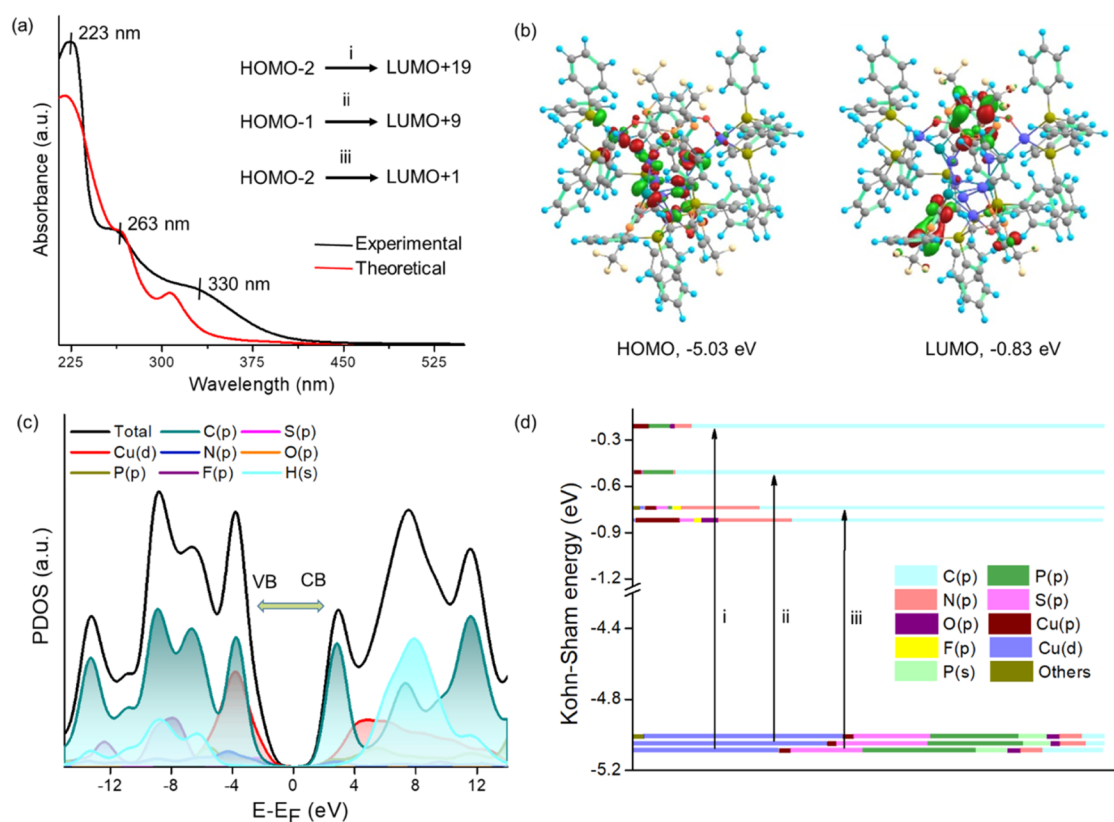


Figure 3. (a) Experimental absorption spectrum (black) of Cu_8 nanocluster and correlation with the theoretical spectrum (red); inset shows electronic transitions associated with the respective absorption features. (b) HOMO and LUMO of Cu_8 nanocluster. (c) Projected density of states of Cu_8 nanocluster with respect to individual atomic orbitals (VB = valence band and CB = conduction band). (d) KS energy diagram of the cluster representing the electronic transitions.

and $-\text{OH}$ ($\sim 3170\text{ cm}^{-1}$) peaks was not observed in FTIR of the cluster confirming the thiol bound to the metal core through S and O sites.

Theoretical Understanding of the Electronic Structure. Time-dependent density functional theory (TDDFT) has been carried out using B3LYP and 6–31G* level of theory implemented in the Gaussian 09 package to gain insights into electronic energy levels and associated optical properties of the cluster.⁴¹ The simulated UV–vis spectrum is in good agreement with the experimental spectrum of the cluster dissolved in acetonitrile (Figure 3a). TDDFT reveals three distinct optical absorption peaks (at 223, 263, and 330 nm), which are due to transitions of HOMO – 2 \rightarrow LUMO + 19 (5.61 eV/221 nm), HOMO – 2 \rightarrow LUMO + 9 (4.68 eV/265 nm), and HOMO – 2 \rightarrow LUMO + 1 (3.92 eV/316 nm), respectively, as mentioned in Figure S10. The electron density maps of these molecular orbitals, along with the Kohn–Sham (KS) molecular orbital analysis indicate that the electronic transitions primarily occur from the core d and p orbitals of Cu and S, respectively, to the p orbitals of C and N in the ligand region. To gain better insights into the electronic properties of Cu_8 NC, we have performed a projected density of state (PDOS) analysis using the Vienna Ab initio Simulation Package.⁴² The valence band edges are dominated by the Cu(d) state; on the other hand, the conduction band edges are dominated by the states of ligand (specifically C) of the Cu_8 NC. This finding aligns well with the TDDFT analysis and altogether suggests a possibility of core-to-ligand transitions.

Formation of Cluster-Assembled Spheroids and Photophysical Properties.

A mixed solvent strategy was used for the preparation of luminescent spheroidal assemblies with a range of nanometric dimensions (Figure 4e). Literature suggests that such an assembly by MNCs is energetically favorable, as shown by molecular dynamics (MD) studies.⁴³ Cu_8 NCs are stabilized by a combination of hydrophobic and hydrophilic ligands (thiol and phosphine) and are well dispersed in DMF. When water is added to the cluster in DMF, the polarity of the local environment changes, which drives the aggregation of such clusters leading to stable noncovalent interactions (C–H $\cdots\pi$, $\pi\cdots\pi$, CH \cdots F, etc.) forming spheroidal assemblies. The formation of such spherical morphology of cluster-assembled structures is possibly due to the minimization of surface energy.^{44,45} We have performed additional self-assembly experiments to show the role of other polar protic solvents (methanol/MeOH, ethanol/EtOH, *n*-propanol/*n*-PrOH, *n*-butanol/*n*-BuOH, and *t*-Butanol/*t*-BuOH, 80% volume fraction of solvents). In all cases, we found no assembly formation, which does not result in any emission under UV (Figure S11). Based on these experiments, we anticipated that the polarity of the medium (dielectric constant for water) plays a key role in forming such assembled spheroids. Dynamic light scattering (DLS) measurement shows a larger size of aggregates as the volume % of water is increased up to 80% (Figure S12). FESEM shows the growth and size of such spheroids with different dimensions (Figure S13). Transmission electron microscopy (TEM) image shows the spheroid shape of aggregates (Figure S14). The restriction

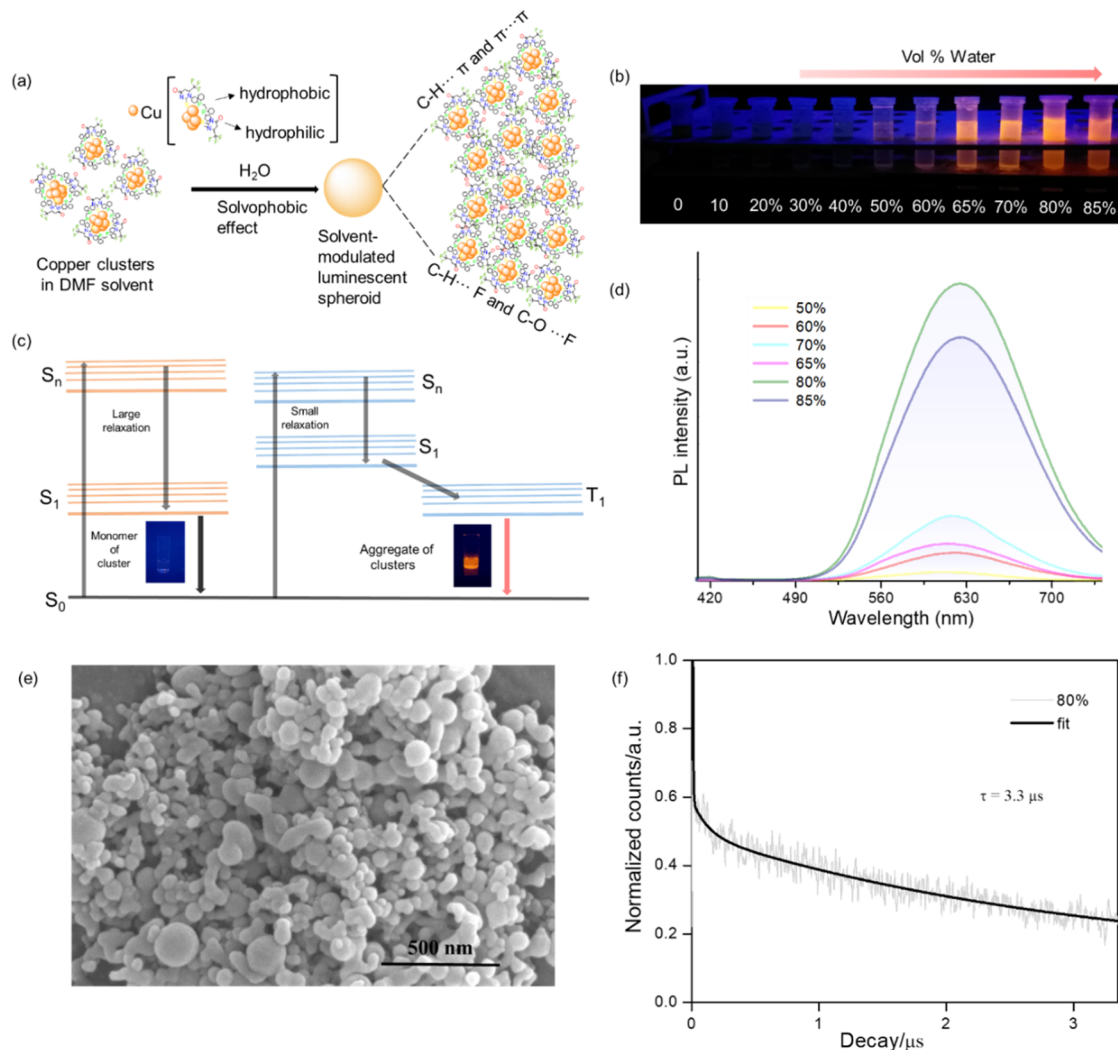


Figure 4. (a) Schematic illustration of the assembly of clusters within the spheroids. (b) A photograph of the samples in volume % of water under UV light exposure, showing the solvent-induced aggregation property of the cluster. (c) A schematic diagram distinguishing PL decay pathways of monomeric clusters and aggregates. (d) PL spectra at different volume % of water. (e) FESEM shows the morphology of as-synthesized spheroids (80% volume fraction of water) and (f) TCSPC decay curve of aggregates (80% volume fraction of water).

of molecular vibrations and rotations within these spheroids enhances their radiative decay, which leads to an orange emission. Generally, the aggregated clusters have different excited states PL and lifetimes compared with monomeric clusters, which enrich their photophysical properties.^{46,47} Time-correlated single-photon counting (TCSPC) measurements show that CASs exhibit phosphorescence with lifetimes of τ_{avg} 3.3 μs /80%, τ_{avg} 2.6 μs /85%, τ_{avg} 0.7 μs /60%, and τ_{avg} 0.7 μs /50% (Figure S15), with volume % of water mentioned in each case. The effect of pH on the luminescence of CASs (using an 80% volume fraction of water) was monitored. The as-prepared CASs show pH-switchable orange emission (Figure S16). The emission feature vanished at pH \sim 10, which reappeared at pH \sim 5 (using sodium hydroxide and acetic acid, respectively). A red shift (\sim 5 nm) with an increase in PL intensity was observed by changing the pH of the solution from 10 to 5.

The pH-triggered luminescence reversibility was monitored for up to 5 cycles by altering the pH (from 10 to 5, or vice versa) of the solution (Figure S16b). The pH-induced modulation in PL properties is possibly due to the charge transfer phenomenon between metal core and ligand. Upon

protonation of free nitrogen site of bipyrimidine moiety at pH \sim 5, the charge transfer becomes facile, while deprotonation at pH \sim 10 disturbs the charge transfer. The morphology of CASs in pH \sim 10 changes, which may be due to the interaction between cluster and base (Figure S16c).^{49b} PL decay upon oxygen exposure to the luminescent aggregates supports that their emission occurs from the triplet excited state (Figure S17). Such aggregates retain their emission even for up to 30 days (Figure S18). Temperature-dependent PL was measured from room temperature to 200 °C (Figure S19), and it shows a gradual decrease in emission. The powder X-ray diffraction spectrum of synthesized Cu₈ NC was measured using 30 mg of powder sample showing crystallinity behavior similar as predicted from single crystal structure (Figure S24). Thermogravimetric analysis (TGA) and derivative thermogravimetry (DTG) analysis together show that the initial mass loss is due to solvent molecules, and then the major mass loss is due to bond breakage of the cluster (Figure S25).

Volatile Amine Compound Sensing. To expand the application of such luminescent aggregates, a sensing experiment was performed for the detection of amines. They show “turn-off” luminescence in both liquid and vapor states of

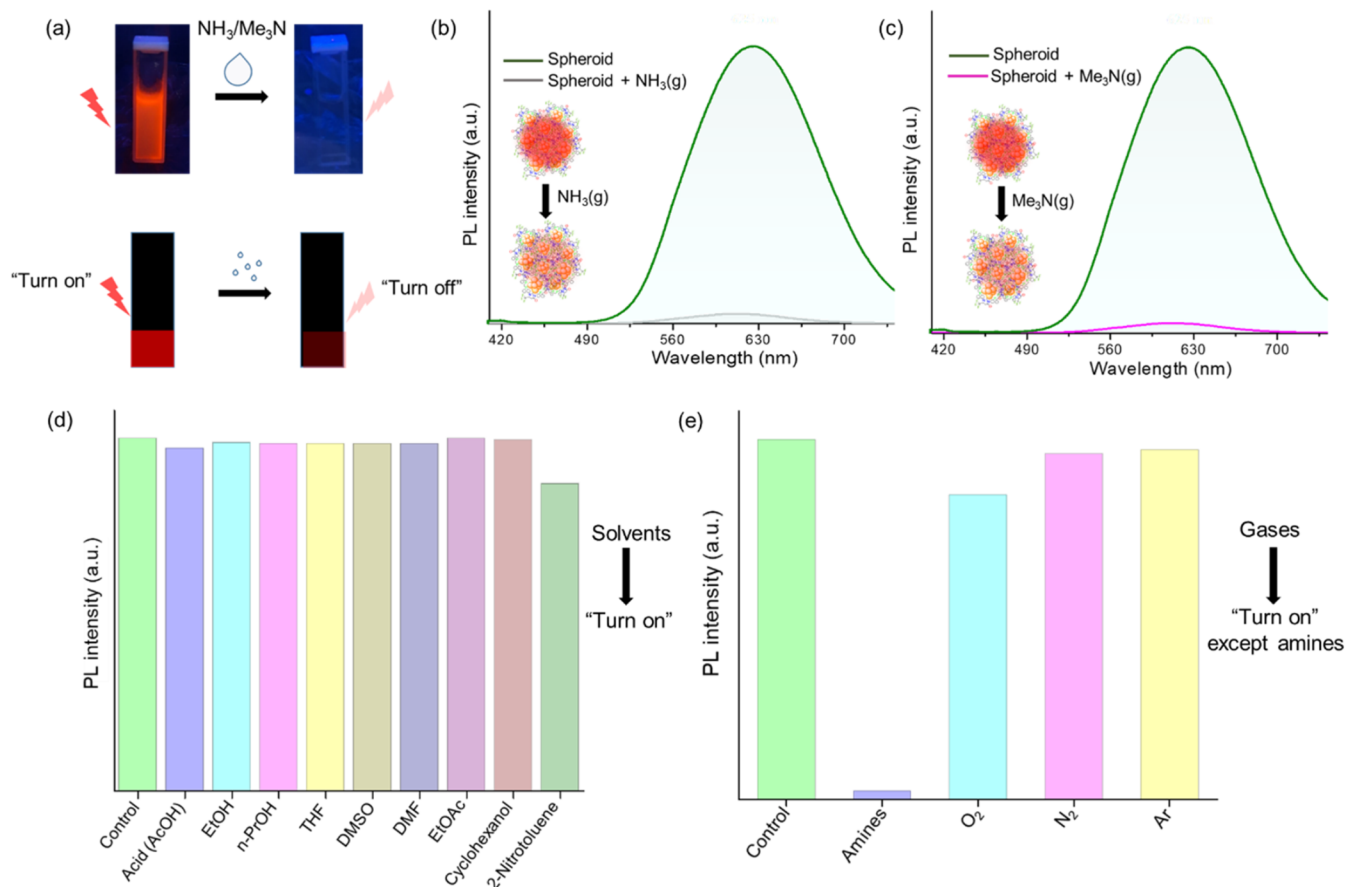


Figure 5. (a) Schematic illustration of luminescence quenching upon ammonia and trimethyl amine (in liquid and vapor) exposure, respectively. (b, c) PL quenching upon amine (NH_3 and NMe_3) exposure, respectively; inset shows representation of spheroids in turn-on and turn-off conditions. (d, e) Bar diagram showing the selectivity to different solvents/acids and other gases, significant quenching was observed for amine vapor.

amines (Figure 5a). To carry out the luminescence quenching experiment, the luminescent aggregates (80% volume fraction of water, ~ 1.5 mg) were drop cast onto a graphite strip (Experimental Section in SI), and it was dried in an air oven (1 h, 40°C). After that, the coated strip was exposed to amine vapor (300 μL of ammonia, trimethyl amine, diethyl amine, dimethyl amine, triethyl amine, and ethylene diamine in a closed container of 15 mL). The emission of CASs was quenched spontaneously in all cases (Figures 5b,c and S20). A detailed study of luminescence quenching was performed on NH_3 and NMe_3 due to their relevance to foodstuffs (fish and chicken) spoilage.⁴⁸ Experiments were also performed to show the material's usability in realistic samples. The freshly prepared luminescent aggregates (80 vol % fraction of water) were drop casted on a strip and dried in oven (50°C for 10 min.). Then the strip was exposed to spoiled fish and chicken kept inside the container (SI, page S3), and no emission of aggregates (365 nm UV light) was observed. The rate of decrease in PL intensity upon amine exposure (Figure S21) was recorded, which suggests that luminescence quenching upon NH_3 vapor exposure occurs more rapidly compared with NMe_3 (8 and 12 min, respectively, Figure S21). Such luminescent CASs can detect NH_3 and Me_3N with an ultralow detection limit of 0.568×10^{-7} M and 0.362×10^{-7} M (0.001 and 0.002 ppm), respectively (Figure S22), which is better or comparable to previous reports on NH_3 and Me_3N sensing by different materials.⁴⁹ UV-vis spectra indicate that

the cluster remains stable after amine (NH_3 and Me_3N) sensing experiments (Figure S23). Further, to check the sensitivity of the material, the emission was measured for a broad range of volatile solvents, nitroaromatics, and other gases, which do not show any significant reduction in the emission intensity (Figure 5d,e). DFT calculations were performed to investigate the "turn-off" luminescence of CASs upon amine (NH_3 and NMe_3) exposure. The calculated adsorption energies for NH_3 and NMe_3 were -0.48 and -0.62 eV, respectively (inset of Figure 6a). These values confirm the spontaneous binding of amines to the surface of the cluster. Additionally, charge density difference (CDD) analysis revealed the charge accumulation on the cluster surface due to bound amines (NH_3 and NMe_3) and Cu_8 NC, respectively (Figure 6b,c). Interaction between cluster and amine possibly causes nonradiative decay leading to "turn-off" luminescence.

CONCLUSIONS

In summary, we have prepared a new Cu_8 nanocluster, primarily protected by a 4-hydroxy-6-(trifluoromethyl) pyrimidine-2-thiol ligand. Copper atoms are arranged in a tetracapped distorted tetrahedral geometry, which makes the core unique over the Cu_8 clusters reported so far. The cluster, as a discrete molecular entity, does not show luminescence in solution and the crystalline state; however, it shows bright luminescence due to the formation of cluster-assembled spheroids upon the addition of water as the antisolvent. The

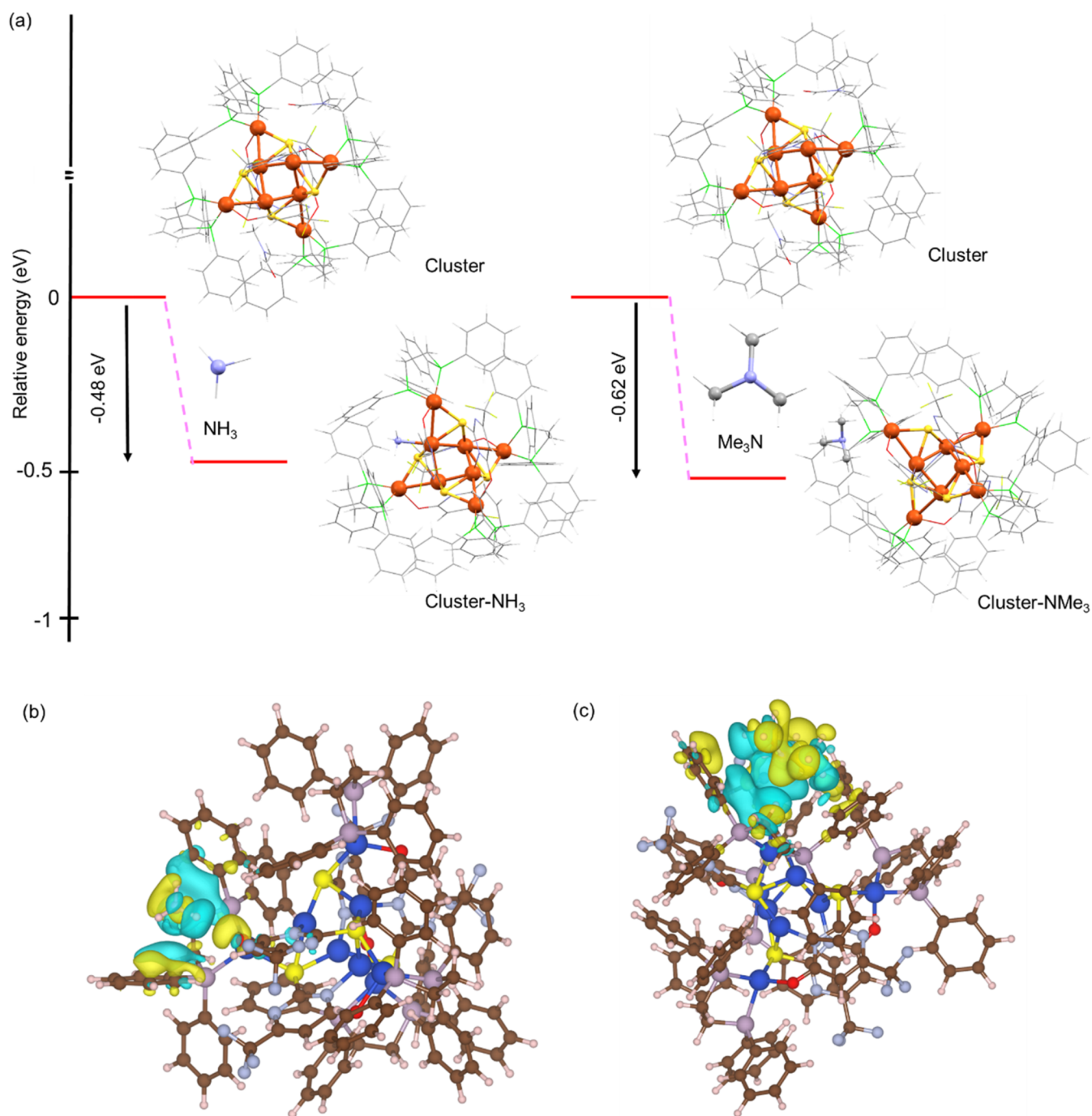


Figure 6. (a) Energetics of the binding of amines (NH_3 and NMe_3) to cluster as revealed by DFT calculation. (b, c) Charge density difference (CDD) due to adsorption on a cluster by NH_3 and NMe_3 , respectively. Atomic color code: orange/blue = Cu, yellow = S, gray = C, red = O, light gray = F, gray with white background = P, and light magenta = H. The yellow and cyan electron density isosurfaces are plotted at a value of $0.00015 \text{ |el } \text{\AA}^{-3}$.

photoluminescence lifetime decay profile shows that the as-synthesized luminescent spheroids are phosphorescent, and their lifetime increases with the amount (50–80 vol %) of water. Such luminescent spheroids were explored exclusively for rapid sensing of volatile amines (NH_3 and Me_3N) with ultralow detection limits of 0.001 and 0.002 ppm, respectively. In conclusion, this work introduces a novel cluster-assembled spheroid featuring a distinctive Cu_3 core structure that exhibits “turn-off” luminescence and fast sensing for volatile amines. This systematic study will help expand interest in such materials.

EXPERIMENTAL SECTION

Materials and Chemicals. Copper iodide (CuI), 1,2-bis-(diphenylphosphino)ethane (DPPE), sodium borohydride (NaBH_4 , 98%), and 4-hydroxy-6-(trifluoromethyl) pyrimidine-2-thiol (TFMPT- H_2) were purchased from Sigma-Aldrich. Potassium bromide (KBr, IR grade) was obtained from Sigma-Aldrich. Milli-Q water was used for purification. High-performance liquid chromatography (HPLC)-grade acetonitrile (ACN), methanol (MeOH), *N,N*-dimethylformamide (DMF), amines (ammonia/25% aqueous, trimethyl amine/30% aqueous, diethyl amine, dimethyl amine, triethyl amine, and ethylene diamine), alcohols (methanol, ethanol, *n*-

propanol, *n*-butanol, *t*-butanol, tetrahydrofuran, and dimethyl sulfoxide), acids (2-chloropropanoic acid and acetic acid), and nitro compound (2-nitrotoluene) were purchased from Rankem and Finar chemicals. All of the reagents and solvents were used without further purification.

Characterization Techniques. A PerkinElmer Lambda 365 UV–vis spectrometer with a bandpass filter of 1 nm was used to record the absorption spectra of the cluster in solution. The mass of nanoclusters (NCs) was measured in a Waters Synapt G2Si high-definition mass spectrometer. The following conditions, a flow rate of 15 $\mu\text{L}/\text{min}$, a capillary voltage of 2.95 kV, a source temperature of 100 $^{\circ}\text{C}$, and a desolvation temperature of 150 $^{\circ}\text{C}$ with a gas flow rate of 400 L/h, were applied for ionization of NCs. The photoluminescence (PL) spectra of spheroidal assemblies were recorded using a Jobin Yvon Nanolog fluorescence spectrometer with a bandpass of 3 nm for excitation and emission. The lifetime of luminescent assemblies was measured using the HORIBA DeltaFlex time-correlated single-photon counting (TCSPC) spectrometer equipped with the detector HORIBA PPD-850 (HORIBA Delta Diode 405 nm laser). Fourier transform infrared spectroscopy was recorded using a PerkinElmer FT-IR JASCO-4100 spectrometer (4 mg of sample in 20 mg of dry KBr). X-ray photoelectron spectroscopy (XPS) of NCs was recorded using an ESCA Probe TPD spectrometer of Omicron Nanotechnology, equipped with a polychromatic Mg $K\alpha$ X-ray source ($h\nu = 1253.6$ eV). The binding energy of different elements was calibrated for C 1s (285.0 eV). Single-crystal X-ray diffraction (SC-XRD) data of single crystals were collected using a Bruker D8 VENTURE instrument equipped with a Cu $K\alpha$ radiation source (1.54 \AA) and a PHOTON II detector. The structure was solved by SHELXT-2018 and refined by full-matrix least-squares techniques using the SHELXL-2018 software package incorporated in the WinGX system version v2018.3. For molecular-level DFT calculations, the Gaussian 09 D.01 program was used. Powder X-ray diffraction data of microcrystalline solids was collected using a D8 Advance Bruker instrument with Cu $K\alpha$ X-ray source of 1.54 \AA . Thermogravimetric (TG) analysis, derivative thermogravimetry (DTG), and differential scanning calorimetry (DSC) measurements of microcrystals were recorded (25–1000 $^{\circ}\text{C}$, N_2 gas flow of 20 mL/min.) using a NETZSCH STA 449 F3 Jupiter instrument equipped with Proteus-6.1.0 software. An optical microscope of LEICA equipped with LAS V4.8 software was used to view the single crystals of NCs at different magnifications and polarization angles. Field emission scanning electron microscopy (FESEM) images of single crystals and their energy-dispersive X-ray spectroscopy analysis were performed with a Verios G4 UC, FEI instrument. Crystals and aggregates were drop cast on the substrate (TEM grid) and dried at room temperature. The sample was then sputter-coated with gold (Au) to produce better-quality images. For transmission electron microscopy (TEM), a Talos F200i instrument operated at 300 kV was used.

Synthesis of $[\text{Cu}_{18}\text{H}_{16}(\text{DPPE})_6]^{2+}$. Cu_{18} nanocluster was synthesized following the procedure available in the literature.³³ For one set of reactions, 95 mg of CuI and 120 mg of DPPE were mixed in 13 mL of ACN, and then the metal ion was reduced with 180 mg of dry NaBH_4 . After 3.5 h of stirring, an orange precipitate was formed. The residue was washed multiple times with ACN and MeOH. Finally, the cluster was dissolved in DCM and used for further studies.

Synthesis of Cu_8 NC. Cu_8 nanocluster was synthesized following the LEIST method using Cu_{18} nanocluster as the precursor. Freshly prepared Cu_{18} NC was dissolved in 4 mL of DMF and then reacted with 15 mg of 4-hydroxy-6-(trifluoromethyl) pyrimidine-2-thiol (TFMPT- H_2) in 1 mL of DMF. After 4 h, the reaction mixture becomes the transparent solution. The as-synthesized cluster was kept for crystallization at room temperature. After 10 days, sheet-like single crystals were grown. The yield of Cu_8 NC is around 70% with respect to the Cu precursor.

Formation of Luminescent Aggregates. To the freshly prepared Cu_8 cluster in the DMF solution, different volume percentage of water was added. After 50% volume fraction of water, luminescence starts appearing in solution due to the formation of cluster-assembled

spheroidal assemblies, as revealed by field emission scanning electron microscopy (FESEM) and dynamic light scattering (DLS) study.

Volatile Amine Compound Sensing. The freshly prepared luminescent aggregates were drop cast on a strip and dried in an oven (50 $^{\circ}\text{C}$ for 10 min). These strips were exposed to a gaseous amine environment. For practical applicability, food spoilage (fish and chicken) was monitored. The experimental setup is mentioned in the Supporting Information.

Computational Details. For molecular-level DFT calculations, the Gaussian 09 D.01 program has been used.^{41a} The Becke's three-parameter hybrid exchange functional and Lee–Yang–Parr's (B3LYP) correlation functional with Pople's 6–31G* basis set were used for nonmetal elements along with LANL2DZ-ECP (effective core potential) for Cu atoms, respectively.^{41f–i} For all of the calculations, an implicit solvation model based on density (SMD) has been adopted for *N,N*-dimethylformamide solvent ($\epsilon = 37.219$) to mimic the experimental conditions.^{41j} In the TDDFT calculations, 500 singlet-to-singlet excitation energies were considered. The Kohn–Sham orbital analysis has been performed using Multiwfn.^{41k}

The Vienna Ab initio Simulation Package (VASP) was employed for periodic boundary condition-based calculations with generalized gradient approximation of Perdew–Burke–Ernzerhof (PBE) functional.^{41l,m} The projector augmented wave (PAW) method was used to treat ion–electron interactions.^{41n–p} The ionic relaxations were carried out using a conjugate gradient algorithm with convergence criteria of 10^{-4} eV and 0.02 eV \AA^{-1} for minimum energy and force, respectively. Owing to the large size of the unit cells of the compounds, the Brillouin zone was sampled at the γ point ($1 \times 1 \times 1$). The charge density differences (CDD) (ρ_{CDD}) have been calculated following eq 1 and plotted using visualization for electronic and structural analysis (VESTA) software.^{41q}

$$\rho_{\text{CDD}} = \rho^{\text{total}} - \sum_i \rho_i^{\text{fragments}} \quad (1)$$

where ρ^{total} is the total charge density of Cu_8NC with adsorbates and $\rho_i^{\text{fragments}}$ is the charge density of the individual fragments.

■ ASSOCIATED CONTENT

Supporting Information

The Supporting Information is available free of charge at <https://pubs.acs.org/doi/10.1021/acs.inorgchem.5c01082>.

Photographs of experimental setup; crystal structure parameters; UV–vis; FESEM; XPS; FTIR; electronic transitions involving HOMO–LUMO; PL and lifetime data; TG and DTG; and associated figures (PDF)

Accession Codes

Deposition Number 2429176 contains the supplementary crystallographic data for this paper. These data can be obtained free of charge via the joint Cambridge Crystallographic Data Centre (CCDC) and Fachinformationszentrum Karlsruhe Access Structures service.

■ AUTHOR INFORMATION

Corresponding Authors

Biswarup Pathak – Department of Chemistry, Indian Institute of Technology Indore, Indore 453552, India; orcid.org/0000-0002-9972-9947; Email: biswarup@iiti.ac.in

Kumaran Nair Valsala Devi Adarsh – Department of Physics, Indian Institute of Science Education and Research Bhopal, Bhopal 462066, India; orcid.org/0000-0002-6337-6545; Email: adarsh@iiserb.ac.in

Thalappil Pradeep – DST Unit of Nanoscience (DST UNS) and Thematic Unit of Excellence (TUE), Department of Chemistry, Indian Institute of Technology Madras, Chennai

600036, India; orcid.org/0000-0003-3174-534X;
Email: pradeep@iitm.ac.in

Authors

Subrata Duary – DST Unit of Nanoscience (DST UNS) and Thematic Unit of Excellence (TUE), Department of Chemistry, Indian Institute of Technology Madras, Chennai 600036, India

Arijit Jana – DST Unit of Nanoscience (DST UNS) and Thematic Unit of Excellence (TUE), Department of Chemistry, Indian Institute of Technology Madras, Chennai 600036, India

Amitabha Das – Department of Chemistry, Indian Institute of Technology Indore, Indore 453552, India; orcid.org/0000-0002-5000-4451

Ankit Sharma – Department of Physics, Indian Institute of Science Education and Research Bhopal, Bhopal 462066, India

Complete contact information is available at:
<https://pubs.acs.org/10.1021/acs.inorgchem.5c01082>

Author Contributions

S.D. carried out the synthesis, crystallization, and the majority of the experimental studies. A.J. contributed to the design of the sensing experiments and participated in writing the manuscript. A.D. conducted the theoretical calculations, while B.P. gave insights into the theoretical data. A.S. measured the photoluminescence (PL) lifetime of the aggregates, and K.N.V.D.A. participated in discussions on the lifetime data. S.D. prepared the first draft of the manuscript and all authors contributed to finalize it. T.P. supervised the work and finalized the manuscript.

Notes

The authors declare no competing financial interest.

ACKNOWLEDGMENTS

S.D. acknowledges the Prime Minister's Research Fellowship (PMRF) from the Government of India (GoI). S.D. thanks the Sophisticated Analytical Instrument Facility, Indian Institute of Technology Madras (SAIF-IITM), for the single-crystal XRD and thermogravimetric (TG) measurements. A.J. acknowledges the financial support from IIT Madras. A.D. thanks GoI for a UGC fellowship. K.N.V.D.A. gratefully acknowledges the Science and Engineering Research Board (Project No. 5 CRG/2023/003013) and the Department of Science & Technology (Project No. DST/NM/TUE/QM-8/2019 342(G)/1). A.S. gratefully acknowledges the UGC for financial support with award No. 1379/(CSIR-UGC NET DECEMBER 2018). T.P. acknowledges funding from the Centre of Excellence (CoE) on Molecular Materials and Functions from the Institute of Eminence scheme of IIT Madras. He thanks the Science and Engineering Research Board (SERB), India, for funding through a research grant (SPR/2021/000439) and a JC Bose Fellowship.

REFERENCES

- (1) Chakraborty, I.; Pradeep, T. Atomically precise clusters of noble metals: emerging link between atoms and nanoparticles. *Chem. Rev.* **2017**, *117* (12), 8208–8271.
- (2) Luo, Z.; Castleman, A. W., Jr; Khanna, S. N. Reactivity of metal clusters. *Chem. Rev.* **2016**, *116* (23), 14456–14492.
- (3) (a) Duary, S.; Jana, A.; Das, A.; Acharya, S.; Kini, A. R.; Roy, J.; Poonia, A. K.; Patel, D. K.; Yadav, V.; Antharjanam, P. S.; Pathak, B.;

et al. Milling-Induced “Turn-off” Luminescence in Copper Nanoclusters. *Inorg. Chem.* **2024**, *63*, 18727–18737. (b) Jana, A.; Jash, M.; Dar, W. A.; Roy, J.; Chakraborty, P.; Paramasivam, G.; Lebedkin, S.; Kirakci, K.; Manna, S.; Antharjanam, S.; Machacek, J.; et al. Carborane-thiol protected copper nanoclusters: stimuli-responsive materials with tunable phosphorescence. *Chem. Sci.* **2023**, *14* (6), 1613–1626.

(4) (a) Chiang, C. H.; Tzeng, Y. W.; Yang, C. I.; Nakano, M.; Wan, W. L.; Lai, L. L.; Lee, G. H. The synthesis of three new Cu₅, Cu₈ and Cu₁₂ clusters via the use of a semi-flexible aminotriazine-based bis-methylpyridine ligand. *Dalton Trans.* **2017**, *46* (4), 1237–1248. (b) Zhang, C.; Wang, Z.; Si, W. D.; Chu, H.; Zhou, L.; Li, T.; Huang, X. Q.; Gao, Z. Y.; Azam, M.; Tung, C. H.; Cui, P.; Sun, D. Dynamic and transformable Cu₁₂ cluster-based CH₃···π-stacked porous supramolecular frameworks. *Nat. Commun.* **2023**, *14* (1), No. 6413.

(5) Jana, A.; Duary, S.; Das, A.; Kini, A. R.; Acharya, S.; Macháček, J.; Pathak, B.; Base, T.; Pradeep, T. Multicolor Photoluminescence of Cu₁₄ Cluster Modulated by Surface Ligands. *Chem. Sci.* **2024**, *15* (34), 13741–13752.

(6) Nematulloev, S.; Huang, R. W.; Yin, J.; Shkurenko, A.; Dong, C.; Ghosh, A.; Alamer, B.; Naphade, R.; Hedhili, M. N.; Maity, P.; Eddaoudi, M.; Mohammed, O. F.; Bakr, O. M. [Cu₁₅(PPh₃)₆(PET)₁₃]²⁺: a copper nanocluster with crystallization enhanced photoluminescence. *Small* **2021**, *17* (27), No. 2006839.

(7) (a) Han, B. L.; Liu, Z.; Feng, L.; Wang, Z.; Gupta, R. K.; Aikens, C. M.; Tung, C. H.; Sun, D. Polymorphism in atomically precise Cu₂₃ nanocluster incorporating tetrahedral [Cu₄] 0 kernel. *J. Am. Chem. Soc.* **2020**, *142* (12), 5834–5841. (b) Nguyen, T. A. D.; Jones, Z. R.; Goldsmith, B. R.; Buratto, W. R.; Wu, G.; Scott, S. L.; Hayton, T. W. A Cu₂₅ nanocluster with partial Cu (0) character. *J. Am. Chem. Soc.* **2015**, *137* (41), 13319–13324.

(8) Ghosh, A.; Huang, R. W.; Alamer, B.; Abou-Hamad, E.; Hedhili, M. N.; Mohammed, O. F.; Bakr, O. M. [Cu₆₁(StBu)₂₆Se₆Cl₆H₁₄]⁺: A Core–Shell Superatom Nanocluster with a Quasi-J₃₆Cu₁₉ Core and an “18-Crown-6” Metal-Sulfide-like Stabilizing Belt. *ACS Mater. Lett.* **2019**, *1* (3), 297–302.

(9) Huang, R. W.; Yin, J.; Dong, C.; Ghosh, A.; Alhilaly, M. J.; Dong, X.; Hedhili, M. N.; Abou-Hamad, E.; Alamer, B.; Nematulloev, S.; Han, Y.; et al. [Cu₈₁(PhS)₄₆(t BuNH₂)₁₀(H)₃₂]³⁺ reveals the coexistence of large planar cores and hemispherical shells in high-nuclearity copper nanoclusters. *J. Am. Chem. Soc.* **2020**, *142* (19), 8696–8705.

(10) Fu, M. L.; Issac, I.; Fenske, D.; Fuhr, O. Metal-Rich Copper Chalcogenide Clusters at the Border Between Molecule and Bulk Phase: The Structures of [Cu₉₃Se₄₂(SeC₆H₄SMe)₉(PPh₃)₁₈], [Cu₉₆Se₄₅(SeC₆H₄SMe)₆(PPh₃)₁₈], and [Cu₁₃₆Se₅₆(SCH₂C₄H₃O)₂₄(dpppt)₁₀]. *Angew. Chem., Int. Ed.* **2010**, *49* (38), 6899–6903.

(11) Ford, P. C.; Cariati, E.; Bourassa, J. Photoluminescence Properties of Multinuclear Copper (I) Compounds. *Chem. Rev.* **1999**, *99*, 3625–3647.

(12) Liu, X.; Astruc, D. Atomically precise copper nanoclusters and their applications. *Coord. Chem. Rev.* **2018**, *359*, 112–126.

(13) Qing, T.; Zhang, K.; Qing, Z.; Wang, X.; Long, C.; Zhang, P.; Hu, H.; Feng, B. Recent progress in copper nanocluster-based fluorescent probing: a review. *Microchim. Acta* **2019**, *186*, No. 670.

(14) Das, N. K.; Mukherjee, S. Size-controlled atomically precise copper nanoclusters: Synthetic protocols, spectroscopic properties and applications. *Phys. Sci. Rev.* **2018**, *3* (11), No. 20170081.

(15) Sharma, S.; Das, S.; Kaushik, K.; Yadav, A.; Patra, A.; Nandi, C. K. Unveiling the Long-Lived Emission of Copper Nanoclusters Embedded in a Protein Scaffold. *J. Phys. Chem. Lett.* **2023**, *14* (40), 8979–8987.

(16) Lin, Y.; Charchar, P.; Christofferson, A. J.; Thomas, M. R.; Todorova, N.; Mazo, M. M.; Chen, Q.; Douth, J.; Richardson, R.; Yarovsky, I.; Stevens, M. M. Surface dynamics and ligand–core interactions of quantum sized photoluminescent gold nanoclusters. *J. Am. Chem. Soc.* **2018**, *140* (51), 18217–18226 2018.

- (17) Wu, Z.; Du, Y.; Liu, J.; Yao, Q.; Chen, T.; Cao, Y.; Zhang, H.; Xie, J. Auophilic Interactions in the Self-Assembly of Gold Nanoclusters into Nanoribbons with Enhanced Luminescence. *Angew. Chem., Int. Ed.* **2019**, *58*, 8139–8144.
- (18) Chakraborty, S.; Bain, D.; Maity, S.; Kolay, S.; Patra, A. Controlling Aggregation-Induced Emission in Bimetallic Gold–Copper Nanoclusters via Surface Motif Engineering. *J. Phys. Chem. C* **2022**, *126*, 2896–2904.
- (19) Wang, S.; Li, Q.; Kang, X.; Zhu, M. Customizing the structure, composition, and properties of alloy nanoclusters by metal exchange. *Acc. Chem. Res.* **2018**, *51* (11), 2784–2792.
- (20) Huang, J. H.; Liu, L. Y.; Wang, Z. Y.; Zang, S. Q.; Mak, T. C. Modular CocrySTALLIZATION of Customized Carboranylthiolate-Protected Copper Nanoclusters via Host–Guest Interactions. *ACS Nano* **2022**, *16* (11), 18789–18794.
- (21) Chakraborty, P.; Nag, A.; Sugi, K. S.; Ahuja, T.; Varghese, B.; Pradeep, T. Crystallization of a supramolecular coassembly of an atomically precise nanoparticle with a crown ether. *ACS Mater. Lett.* **2019**, *1* (5), 534–540.
- (22) Kolay, S.; Bain, D.; Maity, S.; Devi, A.; Patra, A.; Antoine, R. Self-Assembled Metal Nanoclusters: Driving Forces and Structural Correlation with Optical Properties. *Nanomaterials* **2022**, *12*, No. 544.
- (23) Rival, J. V.; Mymoon, P.; Lakshmi, K. M.; Nonappa; Pradeep, T.; Shibu, E. S. Self-Assembly of Precision Noble Metal Nanoclusters: Hierarchical Structural Complexity, Colloidal Superstructures, and Applications. *Small* **2021**, *17*, No. 2005718.
- (24) Bera, D.; Goswami, N. Driving Forces and Routes for Aggregation-Induced Emission-Based Highly Luminescent Metal Nanocluster Assembly. *J. Phys. Chem. Lett.* **2021**, *12*, 9033–9046.
- (25) Wu, Z.; Yao, Q.; Zang, S.; Xie, J. Directed Self-Assembly of Ultrasmall Metal Nanoclusters. *ACS Mater. Lett.* **2019**, *1*, 237–248.
- (26) (a) Wu, Z.; Liu, J.; Gao, Y.; Liu, H.; Li, T.; Zou, H.; Wang, Z.; Zhang, K.; Wang, Y.; Zhang, H.; Yang, B. Assembly-Induced Enhancement of Cu Nanoclusters Luminescence with Mechanochromic Property. *J. Am. Chem. Soc.* **2015**, *137*, 12906–12913. (b) Deng, C. L.; Han, B. L.; Liu, Z. Y.; Pan, Z. H.; He, J.; Li, Y. L.; Yang, Z. L.; Luo, G. G.; Tung, C. H.; Sun, D.; Zheng, L. S. Hierarchical homochiral assembly of polyhedral cage-type nanoclusters. *CCS Chem.* **2024**, *6* (10), 2537–2548.
- (27) Kumar, J. S.; Jana, A.; Raman, J.; Veera, H. M.; Kini, A. R.; Roy, J.; Jana, S. K.; Thomas, T.; Pradeep, T. Cysteine-Protected Antibacterial Spheroidal of Atomically Precise Copper Clusters for Direct and Affordable Arsenic Detection from Drinking Water. *Environ. Sci. Technol. Lett.* **2024**, *11* (8), 831–837.
- (28) Nag, A.; Chakraborty, P.; Thacharon, A.; Paramasivam, G.; Mondal, B.; Bodiuzzaman, M.; Pradeep, T. Atomically precise noble metal cluster-assembled superstructures in water: luminescence enhancement and sensing. *J. Phys. Chem. C* **2020**, *124* (40), 22298–22303.
- (29) Nasrollahpour, H.; Sánchez, B. J.; Sillanpää, M.; Moradi, R. Metal nanoclusters in point-of-care sensing and biosensing applications. *ACS Appl. Nano Mater.* **2023**, *6* (14), 12609–12672.
- (30) Budianto, A.; Pratiwi, A. G.; Ningsih, S. A.; Kusdarini, E. Reduction of Ammonia Nitrogen and Chemical Oxygen Demand of Fertilizer Industry Liquid Waste by Coconut Shell Activated Carbon in Batch and Continuous Systems. *J. Ecol. Eng.* **2023**, *24* (7), 156–164, DOI: 10.12911/22998993/164759.
- (31) Jang, J. K. Amines as occupational hazards for visual disturbance. *Ind. Health* **2016**, *54* (2), 101–115.
- (32) Grant, M. J.; Wolfe, K. M.; Harding, C. R.; Welch, G. C. Biogenic amine sensors using organic π -conjugated materials as active sensing components and their commercialization potential. *J. Mater. Chem. C* **2023**, *11* (29), 9749–9767.
- (33) Li, J.; Ma, H. Z.; Reid, G. E.; Edwards, A. J.; Hong, Y.; White, J. M.; Mulder, R. J.; O'Hair, R. A. Synthesis and X-Ray Crystallographic Characterization of Frustum-Shaped Ligated $[\text{Cu}_{18}\text{H}_{16}(\text{DPPE})_6]^{2+}$ and $[\text{Cu}_{16}\text{H}_{14}(\text{DPPA})_6]^{2+}$ Nanoclusters and Studies on Their H_2 Evolution Reactions. *Chem. - Eur. J.* **2018**, *24* (9), 2070–2074.
- (34) Das, A. K.; Biswas, S.; Wani, V. S.; Nair, A. S.; Pathak, B.; Mandal, S. $[\text{Cu}_{18}\text{H}_{16}(\text{S-Adm})_{12}(\text{PPh}_3)_4\text{Cl}_2]$: fusion of Platonic and Johnson solids through a Cu (0) center and its photophysical properties. *Chem. Sci.* **2022**, *13* (25), 7616–7625.
- (35) Wang, Y. M.; Lin, X. C.; Mo, K. M.; Xie, M.; Huang, Y. L.; Ning, G. H.; Li, D. An Atomically Precise Pyrazolate-Protected Copper Nanocluster Exhibiting Exceptional Stability and Catalytic Activity. *Angew. Chem., Int. Ed.* **2023**, *62* (9), No. 202218369.
- (36) Liao, P. K.; Sarkar, B.; Chang, H. W.; Wang, J. C.; Liu, C. W. Facile entrapment of a hydride inside the tetracapped tetrahedral Cu_8^I cage inscribed in a S_{12} icosahedral framework. *Inorg. Chem.* **2009**, *48* (9), 4089–4097.
- (37) Liu, L. J.; Wang, Z. Y.; Wang, Z. Y.; Wang, R.; Zang, S. Q.; Mak, T. C. Mediating CO_2 electroreduction activity and selectivity over atomically precise copper clusters. *Angew. Chem.* **2022**, *134* (35), No. 202205626.
- (38) Sun, P. P.; Han, B. L.; Li, H. G.; Zhang, C. K.; Xin, X.; Dou, J. M.; Gao, Z. Y.; Sun, D. Real-Time Fluorescent Monitoring of Kinetically Controlled Supramolecular Self-Assembly of Atom-Precise Cu_8 Nanocluster. *Angew. Chem.* **2022**, *134* (20), No. 202200180.
- (39) Xu, Y.; Dong, Q. G.; Dong, J. P.; Zhang, H.; Li, B.; Wang, R.; Zang, S. Q. Assembly of copper-clusters into a framework: enhancing the structural stability and photocatalytic HER performance. *Chem. Commun.* **2023**, *59* (21), 3067–3070.
- (40) Li, H.; Wang, T.; Han, J.; Xu, Y.; Kang, X.; Li, X.; Zhu, M. Fluorescence resonance energy transfer in atomically precise metal nanoclusters by cocrySTALLIZATION-induced spatial confinement. *Nat. Commun.* **2024**, *15* (1), No. 5351.
- (41) (a) Frisch, M. J.; Trucks, G. W.; Schlegel, H. B.; Scuseria, G. E.; Robb, M. A.; Cheeseman, J. R.; Scalmani, G.; Barone, V.; Mennucci, B.; Petersson, G. A. et al. *Gaussian 09, Revision B.01*; Gaussian Inc.: Wallingford, CT, 2009. (b) Mandal, S. C.; Rawat, K. S.; Nandi, S.; Pathak, B. Theoretical insights into CO_2 hydrogenation to methanol by a Mn–PNP complex. *Catal. Sci. Technol.* **2019**, *9* (8), 1867–1878. (c) Becke, A. D. Density-functional thermochemistry. I. The effect of the exchange-only gradient correction. *J. Chem. Phys.* **1992**, *96* (3), 2155–2160. (d) Becke, A. D. Density-functional thermochemistry. IV. A new dynamical correlation functional and implications for exact-exchange mixing. *J. Chem. Phys.* **1996**, *104* (3), 1040–1046. (e) Krishnan, R. B. J. S.; Binkley, J. S.; Seeger, R.; Pople, J. A. Self-consistent molecular orbital methods. XX. A basis set for correlated wave functions. *J. Chem. Phys.* **1980**, *72* (1), 650–654. (f) Becke, A. Density-functional exchange-energy approximation with correct asymptotic behavior. *Phys. Rev. A* **1988**, *38*, No. 3098. (g) Becke, A. D. A new mixing of Hartree-Fock and local density-functional theories. *J. Chem. Phys.* **1993**, *98* (2), 1372–1377. (h) Hehre, W. J.; Ditchfield, R.; Pople, J. A. Self-consistent molecular orbital methods. XII. Further extensions of Gaussian-type basis sets for use in molecular orbital studies of organic molecules. *J. Chem. Phys.* **1972**, *56* (5), 2257–2261. (i) Hariharan, P. C.; Pople, J. A. The influence of polarization functions on molecular orbital hydrogenation energies. *Theor. Chim. Acta* **1973**, *28* (3), 213–222. (j) Marenich, A. V.; Cramer, C. J.; Truhlar, D. G. Universal solvation model based on solute electron density and on a continuum model of the solvent defined by the bulk dielectric constant and atomic surface tensions. *J. Phys. Chem. B* **2009**, *113* (18), 6378–6396. (k) Lu, T.; Chen, F. Multiwfn: A multifunctional wavefunction analyzer. *J. Comput. Chem.* **2012**, *33* (5), 580–592. (l) Perdew, J. P.; Burke, K.; Ernzerhof, M. Generalized gradient approximation made simple. *Phys. Rev. Lett.* **1996**, *77* (18), No. 3865. (m) Adamo, C.; Barone, V. Toward reliable density functional methods without adjustable parameters: The PBE0 model. *J. Chem. Phys.* **1999**, *110* (13), 6158–6170. (n) Mortensen, J. J.; Hansen, L. B.; Jacobsen, K. W. Real-space grid implementation of the projector augmented wave method. *Phys. Rev. B* **2005**, *71* (3), No. 035109. (o) Enkovaara, J.; Rostgaard, C.; Mortensen, J. J.; Chen, J.; Dulak, M.; Ferrighi, L.; Gavnholt, J.; Glinnsvad, C.; Haikola, V.; Hansen, H. A.; Kristoffersen, H. H.; et al. Electronic structure calculations with GPAW: a real-space implementation of the projector-augmented-wave method. *J. Phys.: Condens. Matter* **2010**,

22 (25), No. 253202. (p) Blöchl, P. E. Projector augmented-wave method. *Phys. Rev. B* **1994**, *50* (24), No. 17953. (q) Momma, K.; Izumi, F. VESTA: a three-dimensional visualization system for electronic and structural analysis. *J. Appl. Crystallogr.* **2008**, *41* (3), 653–658.

(42) Kresse, G.; Furthmüller, J. Efficient iterative schemes for ab initio total-energy calculations using a plane-wave basis set. *Phys. Rev. B* **1996**, *54* (16), No. 11169.

(43) (a) Shen, H.; Xu, J.; Fu, Z.; Wei, X.; Kang, X.; Shi, W.; Zhu, M. Photoluminescence Quenching of Hydrophobic Ag₂₉ Nanoclusters Caused by Molecular Decoupling during Aqueous Phase Transfer and Emission Recovery through Supramolecular Recoupling. *Angew. Chem., Int. Ed.* **2024**, *63* (12), No. 202317995. (b) Bhattacharyya, A.; Tiwari, V.; Karmakar, T. Electrostatic-driven self-assembly of Janus-like monolayer-protected metal nanoclusters. *J. Phys. Chem. Lett.* **2024**, *15* (3), 687–692.

(44) Jülicher, F.; Lipowsky, R. Domain-induced Budding of Vesicles. *Phys. Rev. Lett.* **1993**, *70*, No. 2964.

(45) Zhou, Y.; Zeng, H. C. Simultaneous Synthesis and Assembly of Noble Metal Nanoclusters with Variable Micellar Templates. *J. Am. Chem. Soc.* **2014**, *136*, 13805–13817.

(46) Jash, M.; Jana, A.; Poonia, A. K.; Khatun, E.; Chakraborty, P.; Nagar, A.; Ahuja, T.; Adarsh, K. V.; Pradeep, T. Phosphine-Protected Atomically Precise Silver–Gold Alloy Nanoclusters and Their Luminescent Superstructures. *Chem. Mater.* **2023**, *35* (1), 313–326.

(47) Ai, L.; Liu, Z.; Zhou, D.; Liu, J.; Zou, H.; Wu, Z.; Liu, Y.; Zhang, H.; Yang, B. Copper inter-nanoclusters distance-modulated chromism of self-assembly induced emission. *Nanoscale* **2017**, *9* (47), 18845–18854.

(48) Andre, R. S.; Mercante, L. A.; Facure, M. H.; Sanfelice, R. C.; Fugikawa-Santos, L.; Swager, T. M.; Correa, D. S. Recent progress in amine gas sensors for food quality monitoring: novel architectures for sensing materials and systems. *ACS Sens.* **2022**, *7* (8), 2104–2131.

(49) (a) Das, G.; Garai, B.; Prakasam, T.; Benyettou, F.; Varghese, S.; Sharma, S. K.; Gándara, F.; Pasricha, R.; Baias, M.; Jagannathan, R.; Saleh, N. I.; et al. Fluorescence turn on amine detection in a cationic covalent organic framework. *Nat. Commun.* **2022**, *13* (1), No. 3904. (b) D, B.; Dey, D.; Varsha, T. L.; Salfeena, C. T. F.; Panda, M. K.; Somappa, S. B. Rapid visual detection of amines by pyrylium salts for food spoilage taggant. *ACS Appl. Bio Mater.* **2020**, *3* (2), 772–778. (c) Jia, R.; Tian, W.; Bai, H.; Zhang, J.; Wang, S.; Zhang, J. Amine-responsive cellulose-based ratiometric fluorescent materials for real-time and visual detection of shrimp and crab freshness. *Nat. Commun.* **2019**, *10* (1), No. 795. (d) Dalapati, S.; Jin, E.; Addicoat, M.; Heine, T.; Jiang, D. Highly emissive covalent organic frameworks. *J. Am. Chem. Soc.* **2016**, *138* (18), 5797–5800.